Electronic Supplementary Material (ESI) for Physical Chemistry Chemical Physics.

Supplementary Information

Design of lead-free BCZT-based ceramics with enhanced piezoelectric energy harvesting performances

Soukaina Merselmiz,[a,*] Zouhair Hanani,[b] Uroš Prah,[b+] Daoud Mezzane,[a,c] Lahoucine Hajji,[a] Zahra Abkhar,[a] Matjaž Spreitzer,[b] Damjan Vengust,[b] Hana Uršič,[b] David Fabijan,[b] Anna G. Razumnaya,[c,d] Olesia Shapovalova,[e] Igor A. Luk'yanchuk,[c,f] and Zdravko Kutnjak[b]

[a] IMED-Lab, Cadi Ayyad University, Avenue Abdelkrim El Khattabi, P.B. 549, Marrakesh, 40000, Morocco
[b] Jožef Stefan Institute, Jamova cesta 39, Ljubljana, 1000, Slovenia
[c] LPMC, University of Picardy Jules Verne, 33 rue Saint Leu, Amiens, 80039, France
[d] Physics Faculty, Southern Federal University, Rostov-on-Don, 344090, Russia
[e] LAVQ, FCT, Universidade Nova de Lisboa, Campus de Caparica, 2829-516 Caparica, Portugal
[f] Department of Building Materials, Kyiv National University of Construction and Architecture, Kyiv, 03680, Ukraine
[+] Present address: Luxembourg Institute of Science and Technology, 41 rue du Brill, Belvaux, 4422, Luxembourg

[*] Corresponding author: e-mail: soukaina.mers@gmail.com

A. Rietveld refinement of *x*BTSn (0.2≤*x*≤0.6) ceramics

The quantitative phase composition analyses of the *x*BTSn samples were performed using the Rietveld refinement method. For this purpose, the room-temperature XRD patterns were recorded in the 10–80° 2ϑ-range with a step of 0.02°. The EdPCR coupled with WinPLOTR tools in FullProf Suite software was employed. For this purpose, the background (linear interpolation between a set of background points with refinable heights), unit cell parameters, crystallite size, scale factors, sample displacement, atomic coordinates, and thermal parameters were stepwise refined to obtain a calculated diffraction profile that best matched the experimental pattern. The profiles were described using a Pseudo-Voigt function. The fit quality was assessed from the goodness-of-fit parameters R_{wp}, R_{exp}, R_p, R_b, and χ^2. The agreement factors of the Rietveld analysis and the cell parameters of the *x*BTSn ceramics are listed in Table S1, with acceptable residuals of the refinements obtained. The observed relatively high *R*-factors values could be attributed to the conditions of the data collection, such as high counting statistics and background levels.[1] Indeed, the most important way to determine the quality of a Rietveld fit is to graphically check the observed and calculated patterns. Therefore, the enlarged peaks around 2ϑ=32°, 38°, and 45° were inserted in Fig. S1.

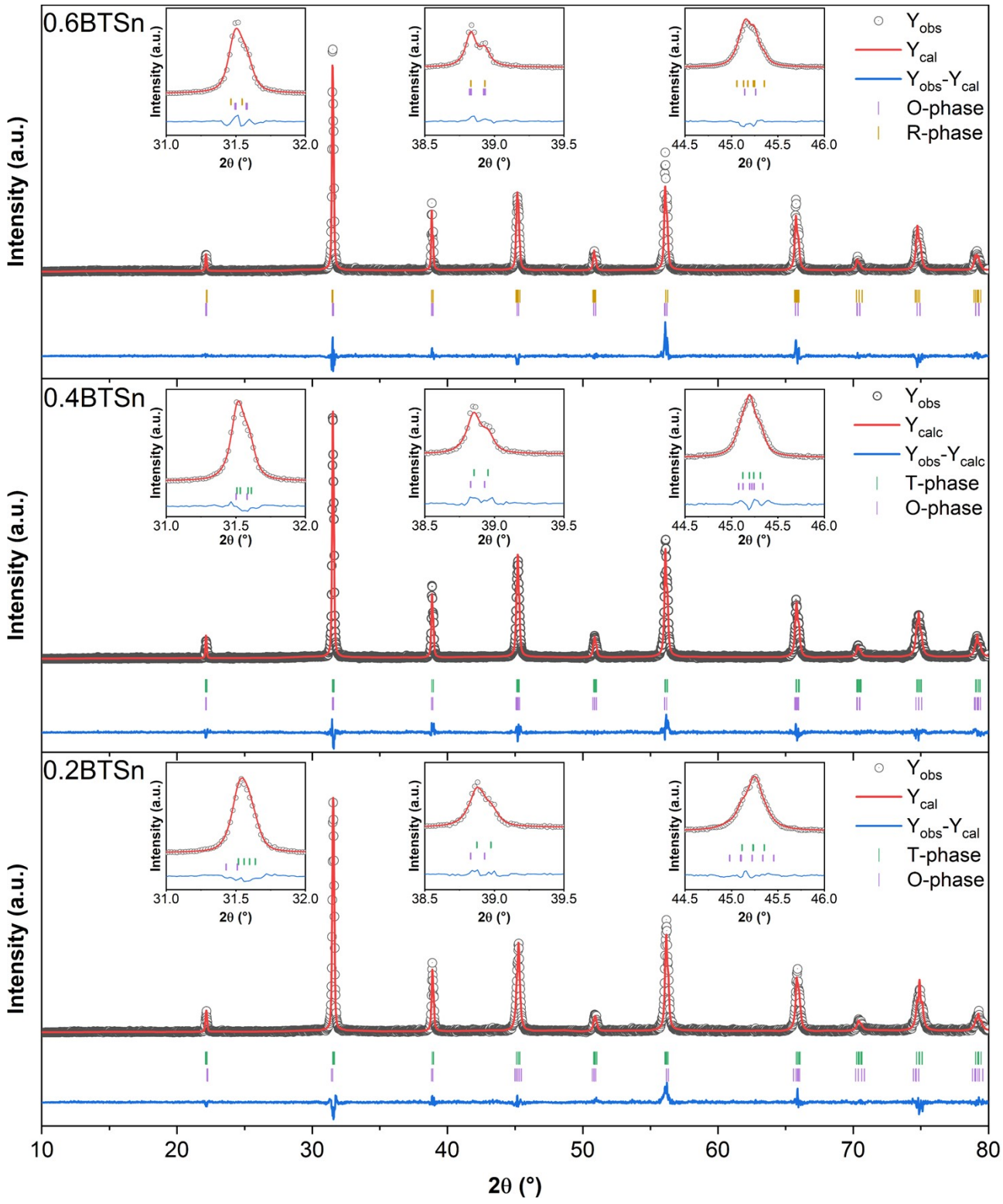

Fig. S1. Rietveld refinement analysis of *x*BTSn (0.2≤*x*≤0.6) ceramics (in insets, the enlarged peaks around 2ϑ=32°, 38°, and 45°).

Table S1. Refined structural parameters for *x*BTSn (0.2≤*x*≤0.6) ceramics.

Composition	**0.2BTSn**		**0.4BTSn**		**0.6BTSn**	
Crystal system	Tetragonal	Orthorhombic	Tetragonal	Orthorhombic	Orthorhombic	Rhombohedral
Space group	*P4mm*	*Amm2*	*P4mm*	*Amm2*	*Amm2*	*R3m*
Weight fraction (%)	79.89	20.11	50.61	49.39	33.51	66.49
***a* (Å)**	4.0059(5)	3.9986(9)	4.0096(8)	4.0133(1)	4.0056(2)	4.0136(2)
***b* (Å)**	4.0059(5)	4.0294(6)	4.0096(8)	4.0212(5)	4.0200(5)	4.0136(2)
***c* (Å)**	4.0153(2)	4.0033(1)	4.0157(9)	4.0066(3)	4.0147(5)	4.0136(2)
***V* (Å^3)**	64.43(6)	64.50(1)	64.56(4)	64.66(1)	64.64(8)	64.65(6)
R_{wp} (%)	19.1		18.7		20.9	
R_{exp} (%)	13.63		14.41		13.68	
R_p (%)	15.0		14.1		17.6	
R_b (%)	7.53	6.27	3.54	5.37	5.81	8.00
χ^2	1.96		1.69		2.34	

B. Temperature-dependent Raman spectroscopy of *x*BTSn (0.2≤*x*≤0.6) ceramics

For all *x*BTSn ceramics, the peak position and intensity of the Raman modes present a decreasing trend with increasing temperature, along with the attenuation of the Raman modes. However, from Fig. S2(a–c), reliable identification of the temperatures corresponding to the structural phase transitions, i.e., FE–PE phase transition, is challenging. Therefore, 2D color maps of the Raman spectra of *x*BTSn samples were obtained using Origin Lab, and the corresponding results are collected gathered in Fig. S2(d–f). At first sight, it is noticeable that the data show a much larger signal at low temperature than at high temperature, and the abrupt color change from yellow to green corresponds to the FE–PE phase transition, although more precise conclusions are required. For this purpose, it was found that the peak around 294 cm^{-1} is characteristic of the ferroelectric phase of $BaTiO_3$-based materials.[2] Hence, considerable attention was paid to the structural phase evolution in *x*BTSn ceramics. The 2D color maps of the Raman spectra of the *x*BTSn samples of E(TO_2) Raman mode are shown in Fig. S2(g–i). For all samples, the intensity of the E(TO_2) mode decreases with increasing temperature and a merging shape was observed. At high temperatures, the abrupt change in data intensity at the peak summit designates

the structural change from ferroelectric to paraelectric phase.[3,4] This time, the phase transitions FE–PE are seen as marked by the dashed line. According to the Raman analyses, this phase transition occurs at around 90, 80 and 70 °C in 0.2BTSn, 0.4BTSn and 0.6BTSn, respectively.

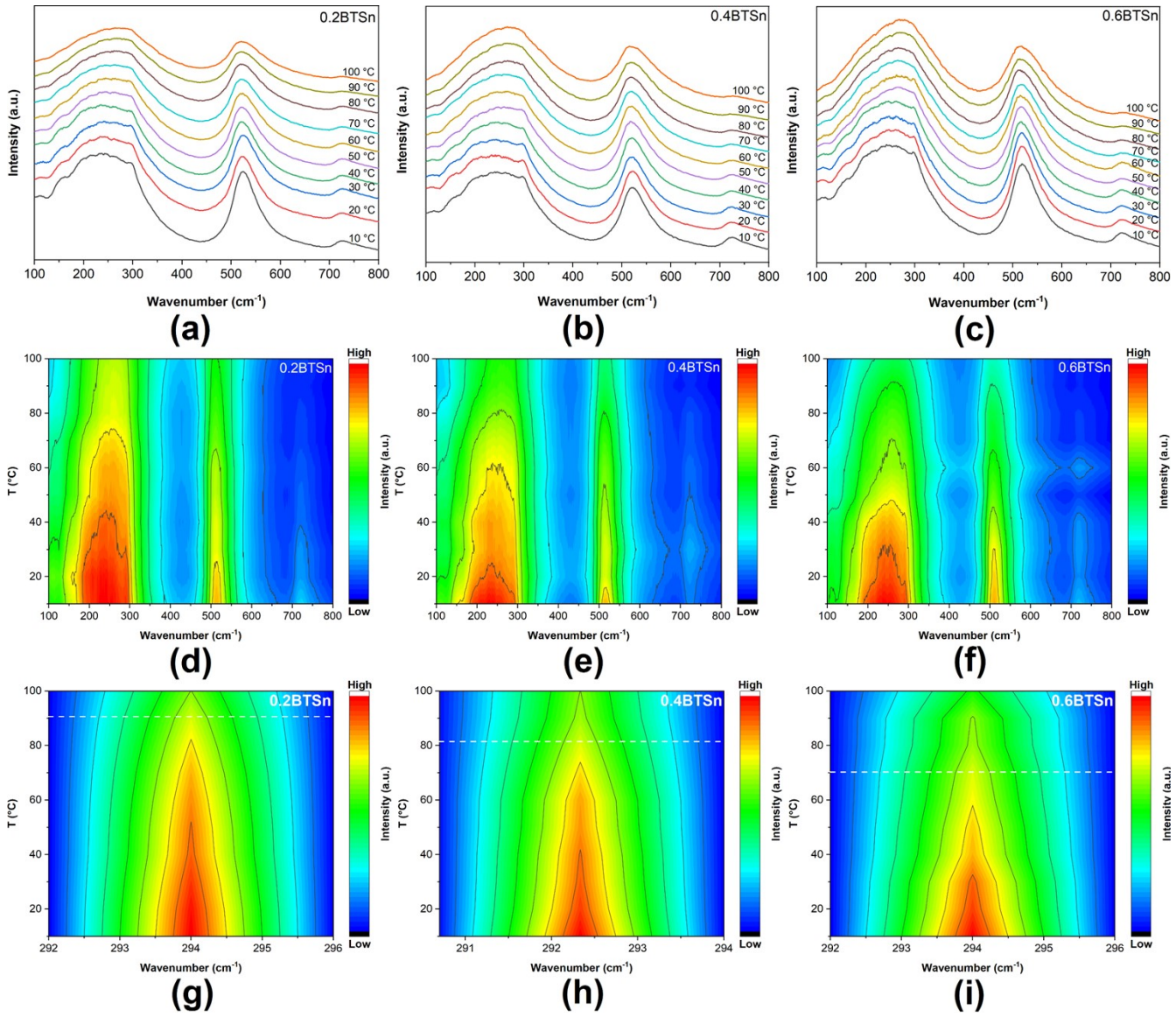

Fig. S2. (a–c) Temperature-dependence of Raman spectra, 2D color map of (d–f) the entire Raman spectra and (g–i) around the E(TO_2) Raman mode of *x*BTSn (0.2≤*x*≤0.6) ceramics.

C. Morphological characteristics of *x*BTSn (0.2≤*x*≤0.6) ceramics

FESEM was performed to observe the morphological characteristics of BTSn addition. The grain morphology and grain size (GS) distribution of the *x*BTSn ceramics are illustrated in Fig. S3 (a–c). All samples exhibit non-uniform grain shape and size distribution. Clear grain boundaries and coarse grains were observed when BTSn was introduced. The coarse grains are surrounded by incipient melting regions at the grain boundaries, which replace the pores formed during sintering and densify the samples' microstructure (Fig. S3b). The grain size increases with the addition of BTSn, which is due to the smaller ionic radii of Sn^{4+} (0.690 Å) compared to Zr^{4+} (0.720 Å) in the B-sites[5,6] Even a small amount of Sn^{4+} can increase the diffusion rate, leading to the high mobility of ions.[7] As a result, the interdiffusion motion through the grain boundaries induced by the formation of necks between the grains leads to rapid grain growth, as shown in Fig. S3a and b.[8] Moreover, all *x*BTSn samples are dense, ranging from 91.6% to 94.6% of the theoretical density (see Table S2). It is well known that the electrical properties of a material are strongly related to the microstructure. Accordingly, a dense microstructure together with a suitable grain size can promote the electrical properties of ceramics.[9]

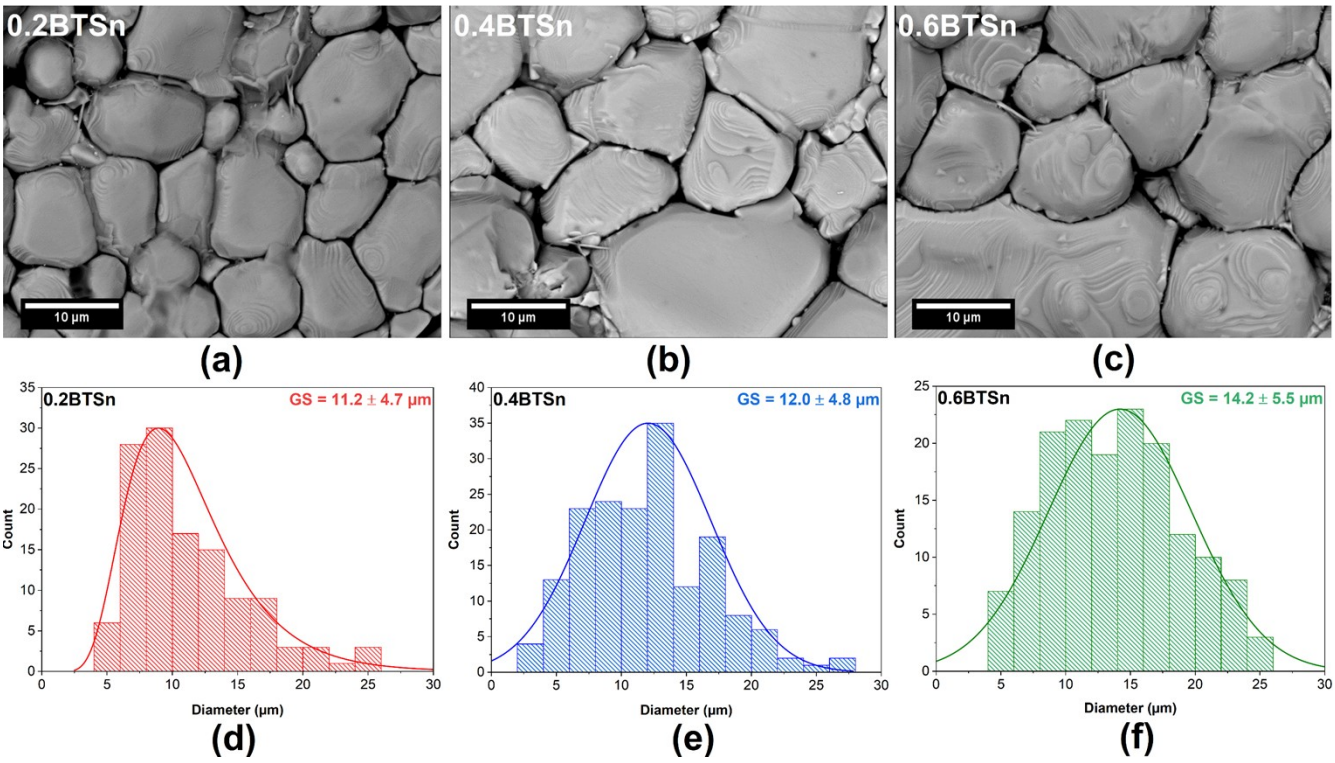

Fig. S3. (a–c) FESEM micrographs of etched surface and (d–f) grain size distributions of *x*BTSn ceramics.

Table S2. Average grain size, bulk, theoretical and relative densities of *x*BTSn ceramics.

Sample	0.2BTSn	0.4BTSn	0.6BTSn
Average grain size (μm)	11.2±4.7	12.0±4.8	14.2±5.5
Bulk density (g/cm³)	5.35	5.48	5.62
Theoretical density (g/cm³)	5.84	5.92	5.94
Relative density (%)	91.6	92.6	94.6

D. Dielectric properties of *x*BTSn (0.2≤*x*≤0.6) ceramics

D.1. Broadening of the dielectric peak temperature

The dielectric peak was normalized from −20 to 150 °C for each *x*BTSn sample to visualize the broadening effect of BTSn addition. The full width at half maximum (FWHM) was reduced from 63.2 to 51.6 °C by the addition of BTSn, due to the convergence of the FE–FE and FE–PE phase transitions, as shown in Fig. S4. This trend was also observed in the (1−*x*)Ba($Ti_{0.89}Sn_{0.11}$)O_3–*x*($Ba_{0.7}Ca_{0.3}$)TiO_3 system.[10]

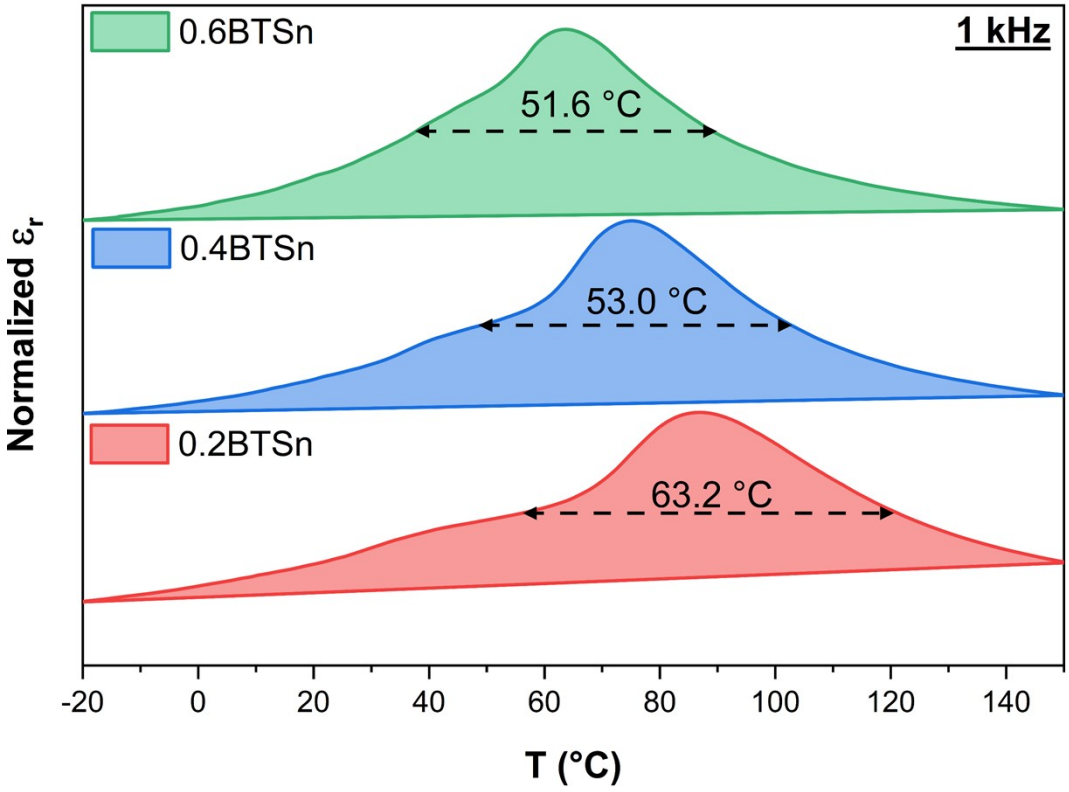

Fig. S4. Normalized ε_r showing the broadening of the dielectric peak temperature of *x*BTSn (0.2≤*x*≤0.6) ceramics.

D.2. Relaxor behavior

In the paraelectric phase, ferroelectric materials regularly obey the Curie–Weiss law, according to Eqn. (1),[11] where ε_r is the relative permittivity constant, T_0 is the Curie–Weiss temperature and C is the Curie-Weiss constant. The reciprocal of ε_r was displayed in Fig. S5 (a–c) as a function of temperature at 1 kHz and fitted by the Curie–Weiss law for all compositions. The result of the fitting is shown in Table S3. In addition, the parameter ΔT_m, which describes the degree of deviation of ε_r from the Curie–Weiss law above T_c, was calculated using Eqn. (2):[12]

$$\frac{1}{\varepsilon_r} = \frac{T - T_0}{C}(T > T_0), \qquad (1)$$

$$\Delta T_m = T_{dev} - T_m, \qquad (2)$$

where, T_{dev} denotes the temperature at which ε_r starts to deviate from the Curie–Weiss law, and T_m indicates the temperature at which the ε_r value reaches the maximum. The highest value of ΔT_m was at 38 °C for 0.4BTSn compared to the other compositions. Moreover, the C value is of the order of 10^5 K, indicating a displacive-type ferroelectric such as $BaTiO_3$ (1.7×10^5 K).[13] To describe the diffusivity of the FE–PE phase transition in xBTSn ceramics, the modified Curie–Weiss law was used and fitted using Eqn. (3):[14]

$$\frac{1}{\varepsilon_r} - \frac{1}{\varepsilon_m} = \frac{(T - T_0)^\gamma}{C}(1 < \gamma < 2), \qquad (3)$$

Where ε_m refers to the maximum value of ε_r and γ is taken as the degree of diffusivity of the phase transition. Thus, γ=1 represents a typical ferroelectric behavior according to the Curie–Weiss law and γ=2 describes the complete diffuse phase transition to a relaxor ferroelectric.[15] The insets in Fig. S5(a–c) shows the modified Curie–Weiss law plot, which indicates a relatively enhanced relaxor behavior in 0.4BTSn ceramics.

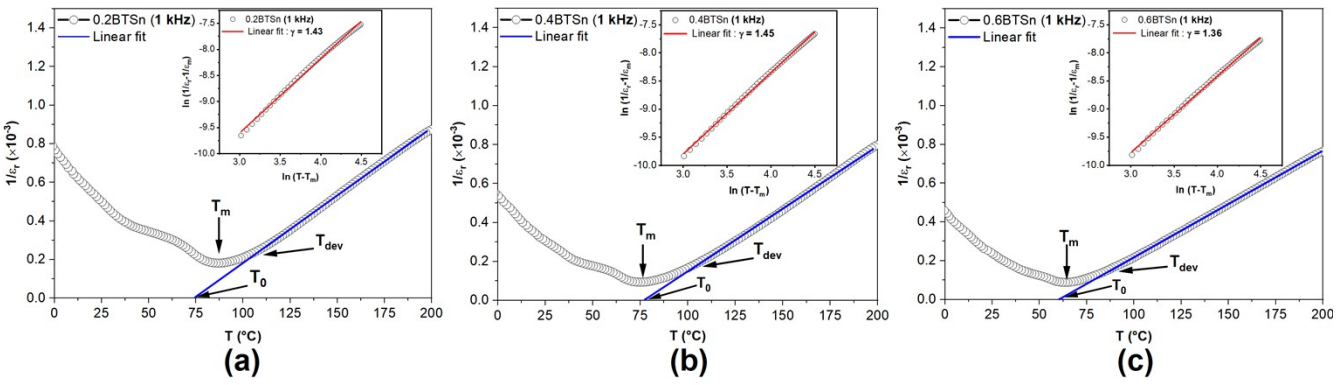

Fig. S5. Thermal evolution of the reciprocal of ε_r at 1 kHz for (a) 0.2BTSn, (b) 0.4BTSn and (c) 0.6BTSn ceramics. Insets: *ln* ($1/\varepsilon_r - 1/\varepsilon_m$) vs. *ln* ($T - T_m$) is plotted at 1 kHz.

Table S3. The dielectric properties of *x*BTSn (0.2≤*x*≤0.6) ceramics at 1 kHz.

Sample	ε_m	*tan δ*	T_0 (°C)	$C \times 10^5$ (K)	T_m (°C)	T_{dev} (°C)	ΔT_m (°C)	γ
0.2BTSn	5,500	0.021	93.4	1.41	87.2	113.5	26.3	1.43
0.4BTSn	10,630	0.031	77.2	1.55	75.3	113.3	38.0	1.45
0.6BTSn	11,270	0.038	60.8	1.81	63.8	93.3	29.5	1.36

E. Ferroelectric properties of *x*BTSn (0.2≤*x*≤0.6) ceramics

E.1. Room-temperature electric field dependence of P–E, J–E and S–E hysteresis loops

Room-temperature *P–E*, *J–E* and *S–E* hysteresis loops of *x*BTSn (0.2≤*x*≤0.6) samples at various electric fields from 10 to 50 kV/cm are shown in Fig. S6. P_{max}, P_r, E_c, J_{max} and S_{max} increase with the increase of the applied electric field. It is worth noting that the negative peak splitting observed in *J–E* tends to merge with increasing the electric field, confirming the orientation of a large number of polar and non-polar regions with the applied electric field direction. Accordingly, an increase in the electric field enhances the ferroelectric properties. It should be noted that the hysteresis loops were not fully saturated at 50 kV/cm; however, the thickness of the samples prevented us from further increasing the electric field.

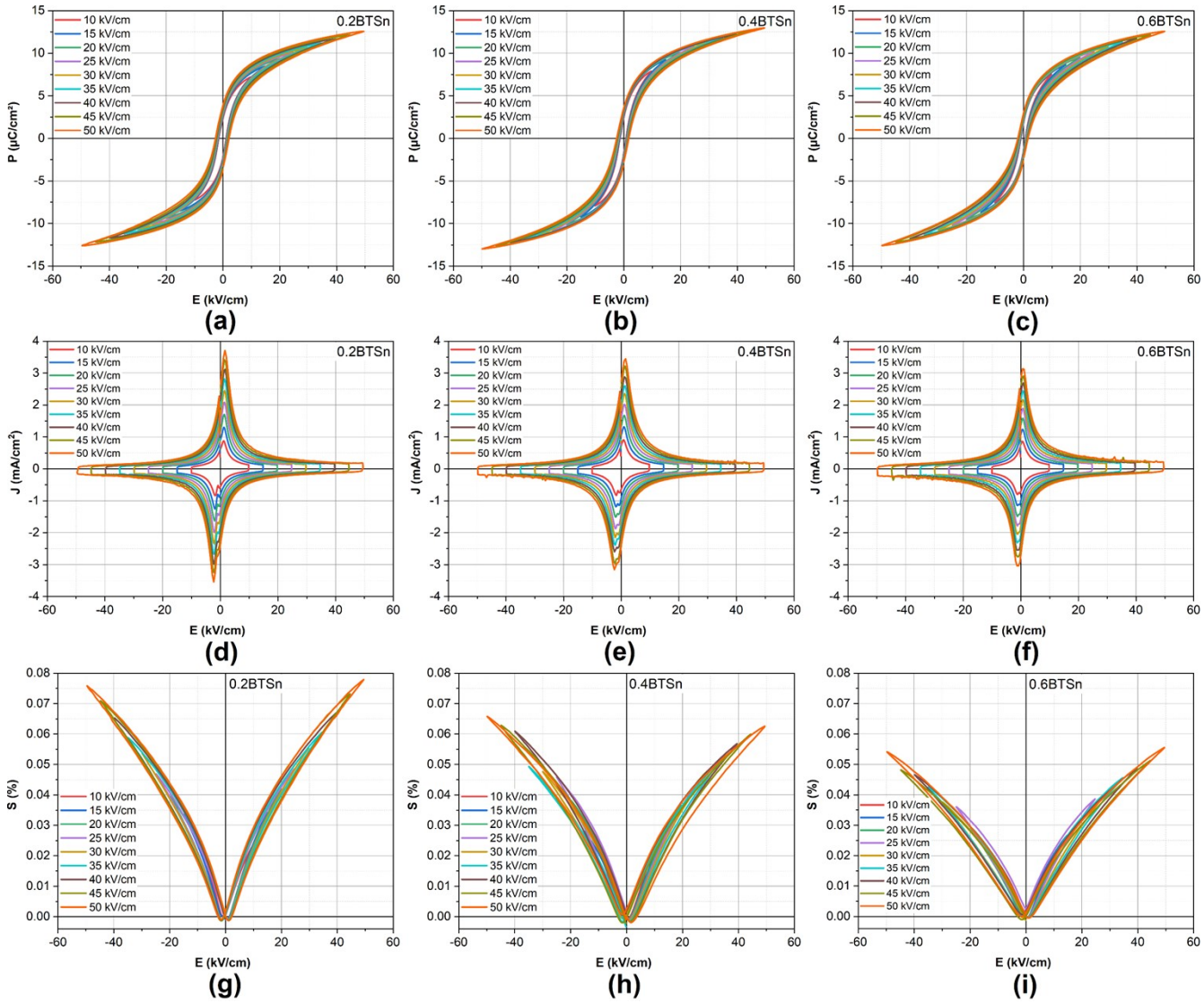

Fig. S6. Room-temperature electric field dependence of (a–c) *P*–*E*, (d–f) *J*–*E* and (g–i) *S*–*E* hysteresis loops of *x*BTSn (0.2≤*x*≤0.6) ceramics.

E.2. Temperature dependence of P–E, J–E and S–E hysteresis loops

Fig. S7 presents the thermal evolution of the *P*–*E*, *J*–*E* and *S*–*E* hysteresis loops of *x*BTSn (0.2≤*x*≤0.6) samples obtained at 25 kV/cm in the temperature range of 30–150 °C. As the temperature increases, the *P*–*E* curves become slimmer due to the disappearance of the ferroelectric domains when crossing the ferroelectric to the paraelectric phase transition, as shown in Fig. S7(a–c). Above T_c, the *P*–*E* loops do not show strictly linear behavior, characteristic of the pure paraelectric phase. In contrast, very slim loops appeared, corresponding to ferroelectric clusters or residual polar nanoregions (PNR), often attributed to the relaxor behavior.[16] It is worth noting that the increase of E_c and P_r in 0.6BTSn ceramics

at higher temperatures can be related to the electrical conductivity. Fig. S7(d–f) also shows the thermal evolution of the *J*–*E* hysteresis loops of *x*BTSn (0.2≤*x*≤0.6) samples. Obviously, increasing the temperature reduced the current peaks, and a flat platform was shown due to the gradual ferroelectric softening, leading to FE–PE state transformation.[4,17] By heating the samples above the Curie temperature, the observed two distinct negative peaks were suppressed (Fig. S7d and e). The temperature dependence of the *S*–*E* hysteresis curves of *x*BTSn samples is plotted in Fig. S7(g–i). As the temperature increases, the maximum strain diminishes gradually, and the *S*–*E* curves become slimmer, demonstrating the paraelectric phase.

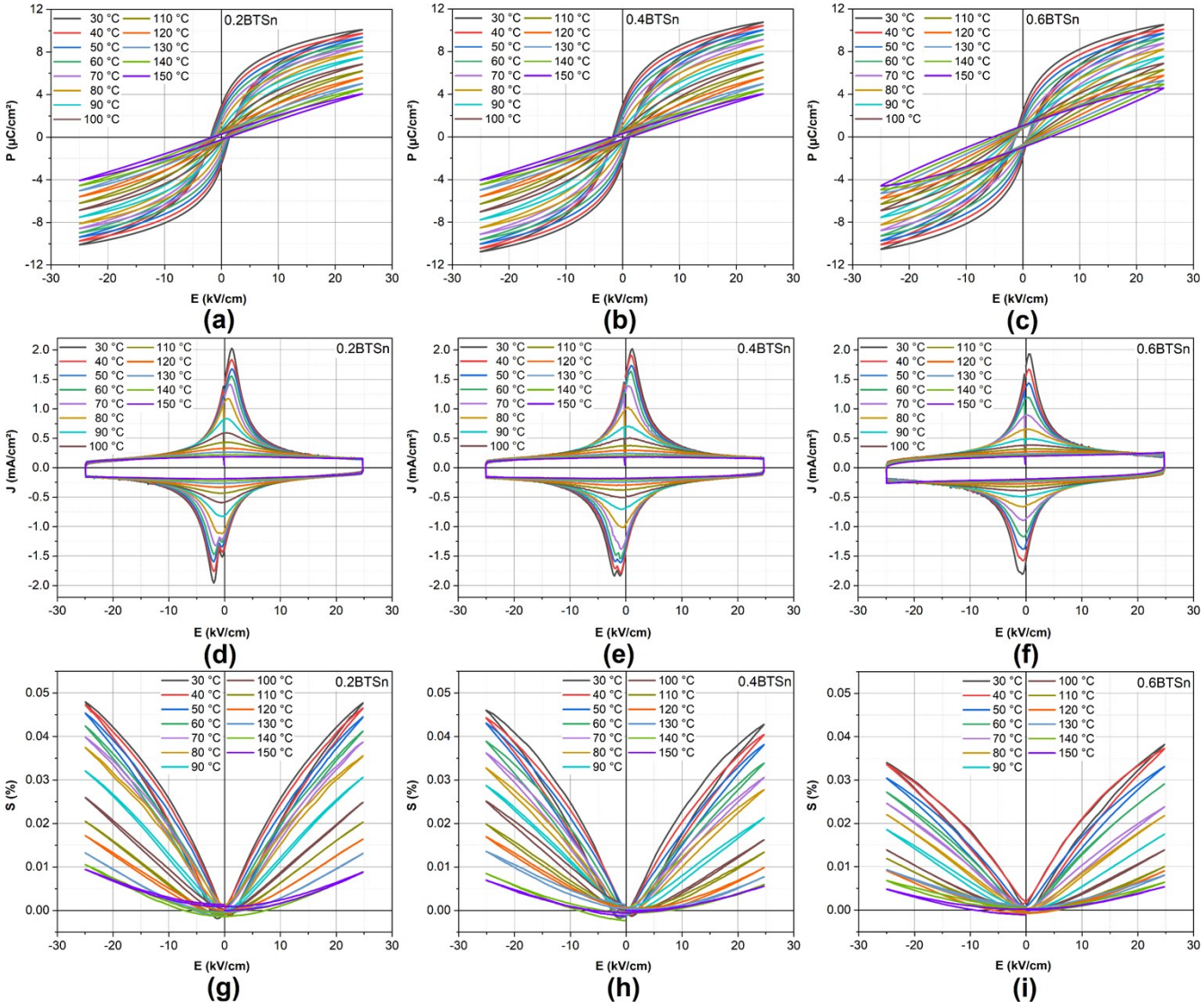

Fig. S7. Temperature dependence of (a–c) *P*–*E*, (d–f) *J*–*E* and (g–i) *S*–*E* hysteresis loops of *x*BTSn (0.2≤*x*≤0.6) ceramics at 25 kV/cm.

F. Piezoelectric properties of *x*BTSn (0.2≤*x*≤0.6) ceramics

F.1. Room-temperature of the piezoelectric properties

Table S4. Comparison of the strain and large-signal piezoelectric coefficient of *x*BTSn ceramics with other lead-free ferroelectric ceramics.

Ceramic	***T*** **(°C)**	S_{max} **(%)**	E_{max} **(kV/cm)**	d_{33}^* **(pm/V)**	**Ref.**
0.2BTSn	30	0.024	10	245	This work
0.4BTSn	30	0.022	10	221	This work
0.6BTSn	30	0.018	10	185	This work
0.2BTSn	30	0.048	25	191	This work
0.4BTSn	30	0.043	25	171	This work
0.6BTSn	30	0.034	25	138	This work
BCZT	30	0.062	25	234	[18]
BTSn	30	0.070	25	280	[19]
$Ba_{0.80}Ca_{0.20}Zr_{0.02}Ti_{0.98}O_3$	30	0.054	25	218	[20]
$Ba_{0.75}Ca_{0.25}TiO_3$	30	0.052	30	173	[21]
$Ba_{0.80}Ca_{0.20}Zr_{0.05}Ti_{0.95}O_3$	30	0.085	30	284	[21]
BZT–52BCT	40	0.076	30	250	[12]
$BaTi_{0.89}Sn_{0.11}O_3$	30	0.083	40	208	[22]
$Ba_{0.85}Ca_{0.15}Zr_{0.08}Ti_{0.92}O_3$	25	0.185	40	463	[23]
$Ba_{0.85}Ca_{0.15}Zr_{0.10}Ti_{0.90}O_3$-0.25Mn	25	0.130	40	325	[24]
BNKT–BST–La_x	25	0.372	60	620	[25]

F.2. Thermal-stability of the piezoelectric properties

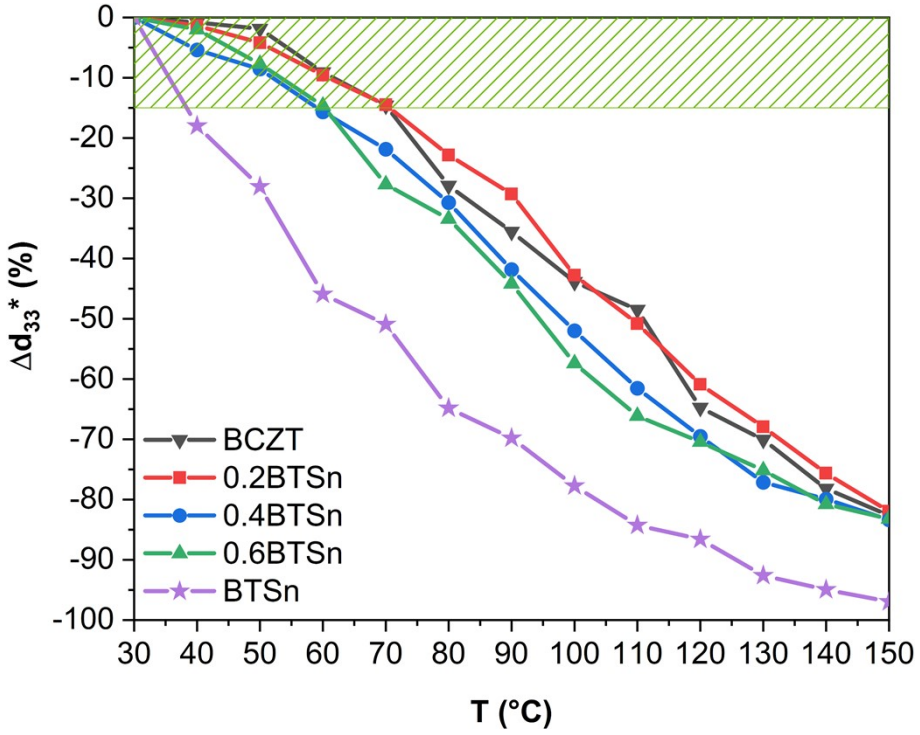

Fig. S8. Thermal stability of the piezoelectric coefficient ($^{\Delta d_{33}^*}$) of BCZT, BTSn and *x*BTSn (0.2≤*x*≤0.6) ceramics between 30 and 150 °C.

G. Piezoelectric energy harvesting performances

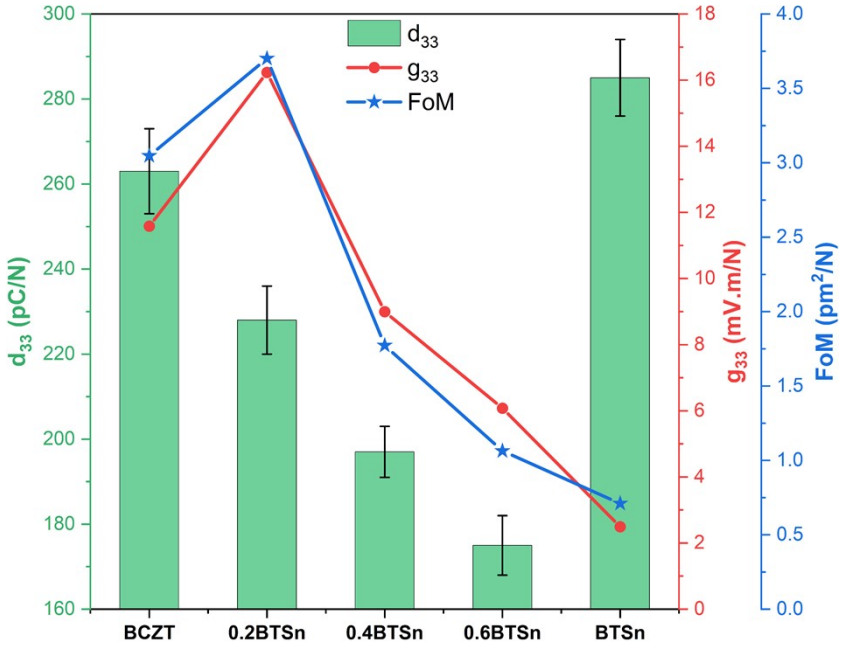

Fig. S9. The plots of d_{33}, g_{33} and *FoM* of BCZT, BTSn, and *x*BTSn (0.2≤*x*≤0.6) ceramics.

References

1 B. H. Toby, R factors in Rietveld analysis: How good is good enough?, *Powder Diffr.*, 2006, **21**, 67–70.

2 B. D. Begg, K. S. Finnie and E. R. Vance, Raman study of the relationship between room-temperature tetragonality and the curie point of barium titanate, *J. Am. Ceram. Soc.*, 1996, **79**, 2666–2672.

3 W. Y. Zeng and A. Anderson, Phase transition behavior of BaZrxTi1-xO3 ceramics, *J. Raman Spectrosc.*, 2001, **32**, 69–71.

4 Z. Hanani, D. Mezzane, M. Amjoud, A. G. Razumnaya, S. Fourcade, Y. Gagou, K. Hoummada, M. El Marssi and M. Gouné, Phase transitions, energy storage performances and electrocaloric effect of the lead-free Ba0.85Ca0.15Zr 0.10Ti0.90O3 ceramic relaxor, *J. Mater. Sci. Mater. Electron.*, 2019, **30**, 6430–6438.

5 M. Chen, Z. Xu, R. Chu, Y. Liu, L. Shao, W. Li, S. Gong and G. Li, Polymorphic phase transition and enhanced piezoelectric properties in (Ba0.9Ca0.1)(Ti1-xSnx)O3 lead-free ceramics, *Mater. Lett.*, 2013, **97**, 86–89.

6 R. D. Shannon, Revised effective ionic radii and systematic studies of interatomic distances in halides and chalcogenides, *Acta Crystallogr. Sect. A*, 1976, **32**, 751–767.

7 J. Shi, X. Lu, J. Shao, B. Fang, S. Zhang, Q. Du, J. Ding, X. Zhao and H. Luo, Effects on structure and properties of BCZT lead-free piezoelectric ceramics by rare-earth doping, *Ferroelectrics*, 2017, **507**, 186–197.

8 K. N. D. K. Muhsen, R. A. M. Osman, M. S. Idris, M. H. H. Jumali and N. H. B. Jamil, Enhancing the dielectric properties of (Ba0.85Ca0.15)(SnxZr0.10−xTi0.90)O3 lead-free ceramics by stannum substitution, *J. Mater. Sci. Mater. Electron.*, 2019, **30**, 20654–20664.

9 Y. Huang, C. Zhao, X. Lv, H. Wang and J. Wu, Multiphase coexistence and enhanced electrical properties in (1-x-y)BaTiO3-xCaTiO3-yBaZrO3 lead-free ceramics, *Ceram. Int.*, 2017, **43**, 13516–13523.

10 C. Zhao, J. Yang, Y. Huang, X. Hao and J. Wu, Broad-temperature-span and large electrocaloric

effect in lead-free ceramics utilizing successive and metastable phase transitions, *J. Mater. Chem. A*, 2019, **7**, 25526–25536.

11 T. Maiti, R. Guo and A. S. Bhalla, The evolution of relaxor behavior in Ti4+ doped BaZrO3 ceramics, *J. Appl. Phys.*, 2006, **100**, 114109.

12 J. P. Praveen, T. Karthik, A. R. James, E. Chandrakala, S. Asthana and D. Das, Effect of poling process on piezoelectric properties of sol-gel derived BZT-BCT ceramics, *J. Eur. Ceram. Soc.*, 2015, **35**, 1785–1798.

13 P. Bharathi and K. B. R. Varma, Grain and the concomitant ferroelectric domain size dependent physical properties of Ba0.85Ca0.15Zr0.1Ti0.9O3 ceramics fabricated using powders derived from oxalate precursor route, *J. Appl. Phys.*, 2014, **116**, 164107.

14 K. Uchino and S. Nomura, Critical exponents of the dielectric constants in diffused-phase-transition crystals, *Ferroelectr. Lett. Sect.*, 1982, **44**, 55–61.

15 S. Hunpratub, S. Maensiri and P. Chindaprasirt, Synthesis and characterization of Ba0.85Ca0.15Ti 0.9Zr0.1O3 ceramics by hydrothermal method, *Ceram. Int.*, 2014, **40**, 13025–13031.

16 Z. Hanani, S. Merselmiz, D. Mezzane, M. Amjoud, A. Bradeško, B. Rožič, M. Lahcini, M. El Marssi, A. V. Ragulya, I. A. Luk'Yanchuk, Z. Kutnjak and M. Gouné, Thermally-stable high energy storage performances and large electrocaloric effect over a broad temperature span in lead-free BCZT ceramic, *RSC Adv.*, 2020, **10**, 30746–30755.

17 Q. Xu, Z. Song, W. Tang, H. Hao, L. Zhang, M. Appiah, M. Cao, Z. Yao, Z. He and H. Liu, Ultra-Wide Temperature Stable Dielectrics Based on Bi0.5Na0.5TiO3-NaNbO3 System, *J. Am. Ceram. Soc.*, 2015, **98**, 3119–3126.

18 S. Merselmiz, Z. Hanani, D. Mezzane, A. G. Razumnaya, M. Amjoud, L. Hajji, S. Terenchuk, B. Rožič, I. A. Luk'yanchuk and Z. Kutnjak, Thermal-stability of the enhanced piezoelectric, energy storage and electrocaloric properties of a lead-free BCZT ceramic, *RSC Adv.*, 2021, **11**, 9459–9468.

19 S. Merselmiz, Z. Hanani, D. Mezzane, M. Spreitzer, A. Bradeško, D. Fabijan, D. Vengust, M. Amjoud, L. Hajji, Z. Abkhar, A. G. Razumnaya, B. Rožič, I. A. Luk'yanchuk and Z. Kutnjak, High energy storage efficiency and large electrocaloric effect in lead-free BaTi0.89Sn0.11O3 ceramic,

Ceram. Int., 2020, **46**, 23867–23876.

20 S. Merselmiz, Z. Hanani, S. Ben Moumen, A. Matavž, D. Mezzane, N. Novak, Z. Abkhar, L. Hajji, M. Amjoud, Y. Gagou, K. Hoummada, D. Črešnar, Z. Kutnjak and B. Rožič, Enhanced electrical properties and large electrocaloric effect in lead-free Ba0.8Ca0.2ZrxTi1−xO3 (x = 0 and 0.02) ceramics, *J. Mater. Sci. Mater. Electron.*, 2020, **31**, 17018–17028.

21 N. Chaiyo, D. P. Cann and N. Vittayakorn, Phase transitions, ferroelectric, and piezoelectric properties of lead-free piezoelectric xBaZrO3–(0.25−x)CaTiO3–0.75BaTiO3 ceramics, *J. Mater. Sci.*, 2015, **50**, 6171–6179.

22 L. Jin, J. Qiao, L. Hou, Y. Tian, Q. Hu, L. Wang, X. Lu, L. Zhang, H. Du, X. Wei, G. Liu and Y. Yan, A strategy for obtaining high electrostrictive properties and its application in barium stannate titanate lead-free ferroelectrics, *Ceram. Int.*, 2018, **44**, 21816–21824.

23 W. Bai, D. Chen, J. Zhang, J. Zhong, M. Ding, B. Shen, J. Zhai and Z. Ji, Phase transition behavior and enhanced electromechanical properties in (Ba 0.85 Ca 0.15)(Zr x Ti 1−x)O 3 lead-free piezoceramics, *Ceram. Int.*, 2016, **42**, 3598–3608.

24 X. Wang, Y. Huan, Y. Zhu, P. Zhang, W. Yang, P. Li, T. Wei, L. Li and X. Wang, Defect engineering of BCZT-based piezoelectric ceramics with high piezoelectric properties, *J. Adv. Ceram.*, 2022, **11**, 184–195.

25 A. Ullah, A. Ullah, I. W. Kim, D. S. Lee, S. J. Jeong and C. W. Ahn, Large Electromechanical Response in Lead-Free La-Doped BNKT-BST Piezoelectric Ceramics, *J. Am. Ceram. Soc.*, 2014, **97**, 2471–2478.